Time-resolved single-particle x-ray scattering reveals electron-density gradients as coherent plasmonic-nanoparticle-oscillation source

Dominik Hoeing,[†,‡] Robert Salzwedel,[¶] Lena Worbs,[§,‖] Yulong Zhuang,[⊥] Amit K. Samanta,[§,†] Jannik Lübke,[§,†,‖] Armando D. Estillore,[§] Karol Dlugolecki,[§] Christopher Passow,[#] Benjamin Erk,[#] Nagitha Ekanayake,[#] Daniel Ramm,[#] Jonathan Correa,[#] Christina C. Papadopoulou,[#] Atia Tul Noor,[#] Florian Schulz,[‖] Malte Selig,[¶] Andreas Knorr,[*,¶] Kartik Ayyer,[*,†,⊥] Jochen Küpper,[*,§,†,‖,‡] and Holger Lange[*,†,‡]

†*The Hamburg Centre for Ultrafast Imaging, Universität Hamburg, 22761 Hamburg, Germany*

‡*Department of Chemistry, Universität Hamburg, 20146 Hamburg, Germany*

¶*Institut für Theoretische Physik, Technische Universität Berlin, 10623 Berlin, Germany*

§*Center for Free-Electron Laser Science CFEL, Deutsches Elektronen-Synchrotron DESY, 22607 Hamburg, Germany*

‖*Department of Physics, Universität Hamburg, 22761 Hamburg, Germany*

⊥*Max Planck Institut for the Structure and Dynamics of Matter, 22761 Hamburg Germany*

#*Deutsches Elektronen-Synchrotron DESY, 22607 Hamburg, Germany*

E-mail: andreas.knorr@tu-berlin.de; kartik.ayyer@mpsd.mpg.de; jochen.kuepper@cfel.de; holger.lange@uni-hamburg.de

Abstract

Dynamics of optically-excited plasmonic nanoparticles are presently understood as a series of sequential scattering events, involving thermalization processes after pulsed optical excitation. One important step is the initiation of nanoparticle breathing oscillations. According to established experiments and models, these are caused by the statistical heat transfer from thermalized electrons to the lattice. An additional contribution by hot electron pressure has to be included to account for phase mismatches that arise from the lack of experimental data on the breathing onset. We used optical transient-absorption spectroscopy and time-resolved single-particle x-ray-diffractive imaging to access the excited electron system and lattice. The time-resolved single-particle imaging data provided structural information directly on the onset of the breathing oscillation and confirmed the need for an additional excitation mechanism to thermal expansion, while the observed phase-dependence of the combined structural and optical data contrasted previous studies. Therefore, we developed a new model that reproduces all our experimental observations without using fit parameters. We identified optically-induced electron density gradients as the main driving source.

Introduction

Plasmonics treats the unique optical excitation of metallic nanoparticles. The plasmon is a collective electron oscillation, associated with highly localized fields. It offers the ultimate spatial and temporal control over light, concentrating electromagnetic energy into nanoscale volumes. Applications range from catalysis and photovoltaics to sensing and quantum optics.[1–5]

Presently, the details of the plasmon decay are intensely discussed. The current consensus is that very energetic "hot" electrons are generated, which are of interest for many applications. These non-equilibrium carriers thermalize via electron-electron scattering and then quickly couple to lattice phonons. The excited lattice finally dissipates the excess energy into the environment.[6–10] A detailed knowledge of these processes is the basis for controlling them for the respective applications. In particular the relaxation dynamics of hot electrons are of interest and as part of that, the coupling to coherent phonon oscillations producing a periodic change in particle dimension, radial "breathing" oscillations.

The temperature of the thermalized hot electron gas can be observed as a contrast in optical transient-absorption (TA) experiments and conclusions on the lattice temperature can be made based on two-temperature models.[9,11] The breathing oscillations of plasmonic nanoparticles are then apparent as additional periodic contrast modulations in the TA spectra[12–14] and the observed dynamics is typically explained by mechanistic descriptions.[9]

However, TA does not allow disentangling the precise temporal onset of the breathing oscillations from the contrast-dominating initial electron dynamics. Consequently, the details of the excitation were previously deduced indirectly. For example, matching the phase of the experimentally observed breathing oscillations and mechanistic descriptions required an additional impulsive excitation source to heat transfer, which was assigned to hot-electron pressure.[15,16] In such descriptions, the different time dependence of the hot electron pressure compared to the one for the lattice expansion

affected the phase of the breathing oscillation. At high pump laser powers, where the hot electron pressure is assumed to be strongest, the change in phase was on the order of up to 45°.[15]

Today, x-ray free-electron lasers (XFELs) provide intense femtosecond x-ray pulses and allow for the time-resolved imaging of nanoparticle shapes, unaffected from electron temperature effects, down to femtosecond timescales.[17–20] An emerging technique to conduct time-resolved XFEL experiments on nanoparticles is single-particle imaging (SPI),[21,22] which combines a large number of diffraction patterns from individual particles into a diffraction volume, which is then inverted to a nanoparticle structure.[22] A major advantage of SPI is the combination of measuring single-particle images, allowing for correcting sample inhomogeneity, with the statistical robustness of a serial measurement. Using ultrashort x-ray pulses also allows to outrun potential radiation damage induced by the x-ray pulses themselves in a diffract-before-destruction process.[23] Acquiring SPI data in a pump-probe fashion then provides a "movie" of the nanoparticle dynamics, i.e., a direct measure of the nanoparticle's structural changes as a function of time.

Here, we exploited XFEL transient small-angle-x-ray-scattering in a single-particle imaging scheme (tSAX-SPI) and TA spectroscopy to unravel the size and electron temperature of gold nanoparticles (AuNP) as a function of time after optical excitation. The combined SPI and TA experimental observations could not be fully explained within established models. The particle expansion started already with the optical excitation pulse and thus occured in the kinetic limit of the electron gas excitation, see Figure 1. This directly confirms the need for an impulsive-excitation source, which is not the lattice temperature rise. However, additional power-dependent TA experiments showed no phase change, contrary to hot-electron pressure based expectations. Our experimental findings were rationalized by calculations based on a combination of the previous, well established model and an additional new source for coherent AuNP size oscillations yielding a consistent picture of all observed aspects of the breathing excitation.[24] Two source terms for the lattice dynamics emerge from the calculations: The optically-

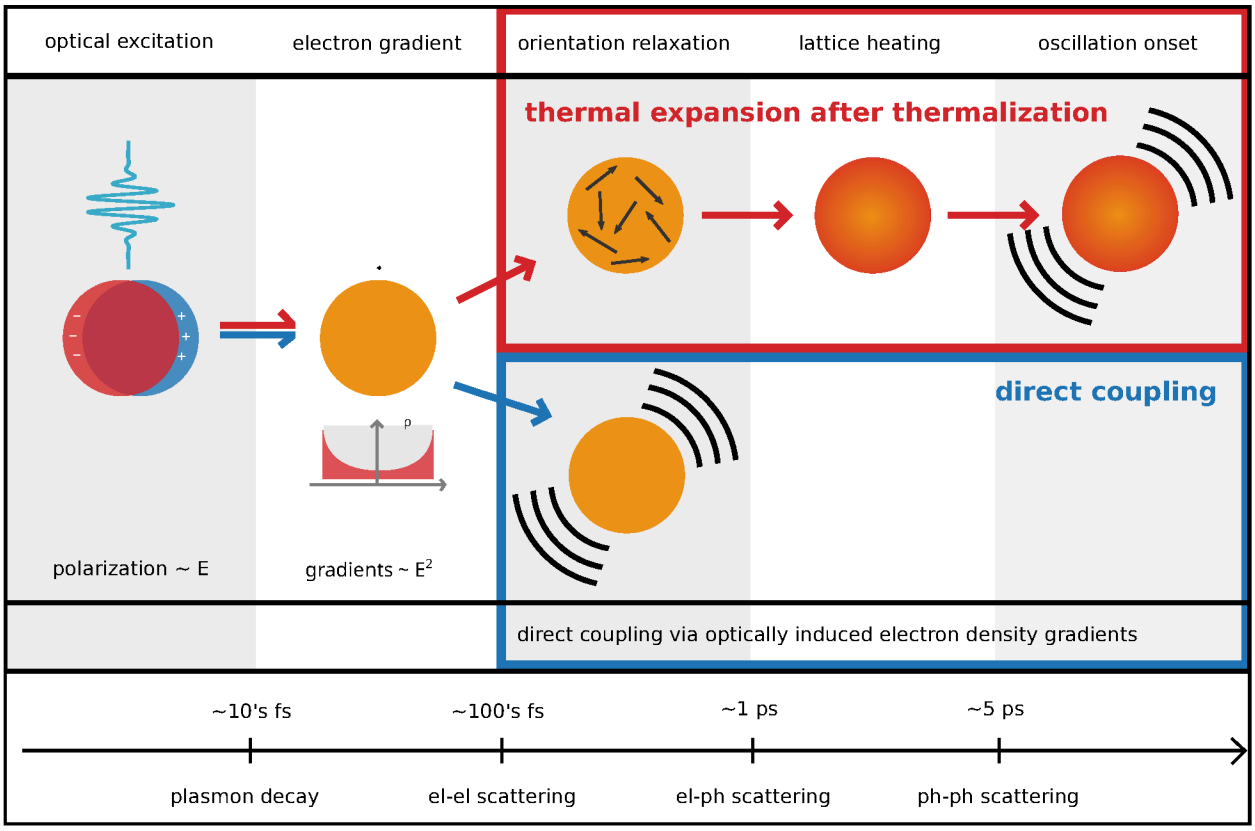

Figure 1: Schematic illustration of the relaxation dynamics in plasmonic nanoparticles: The optical pump causes a polarization of the electrons in the nanoparticle, which is accompanied by a density gradient. The red path illustrates the thermal-driving mechanism of the breathing oscillations: After Coulomb-driven orientation relaxation, electron-phonon scattering converts energy from the electrons to the lattice, which leads to an expansion of the particle. This initiates breathing oscillations. The blue path illustrates the coupling mechanism described in this work, the electron density gradients which directly couple to the coherent phonon mode, impulsively initiating breathing oscillations.

induced spatial gradients of the electron density act as the main initial driving source for the breathing oscillations, accompanied by time-delayed thermal contributions. The dominance of the direct coupling between the displaced electrons and the lattice can have important consequences for applications harnessing hot electrons[2,3,25–27] and for the general understanding of nanoscale metal dynamics.

Results

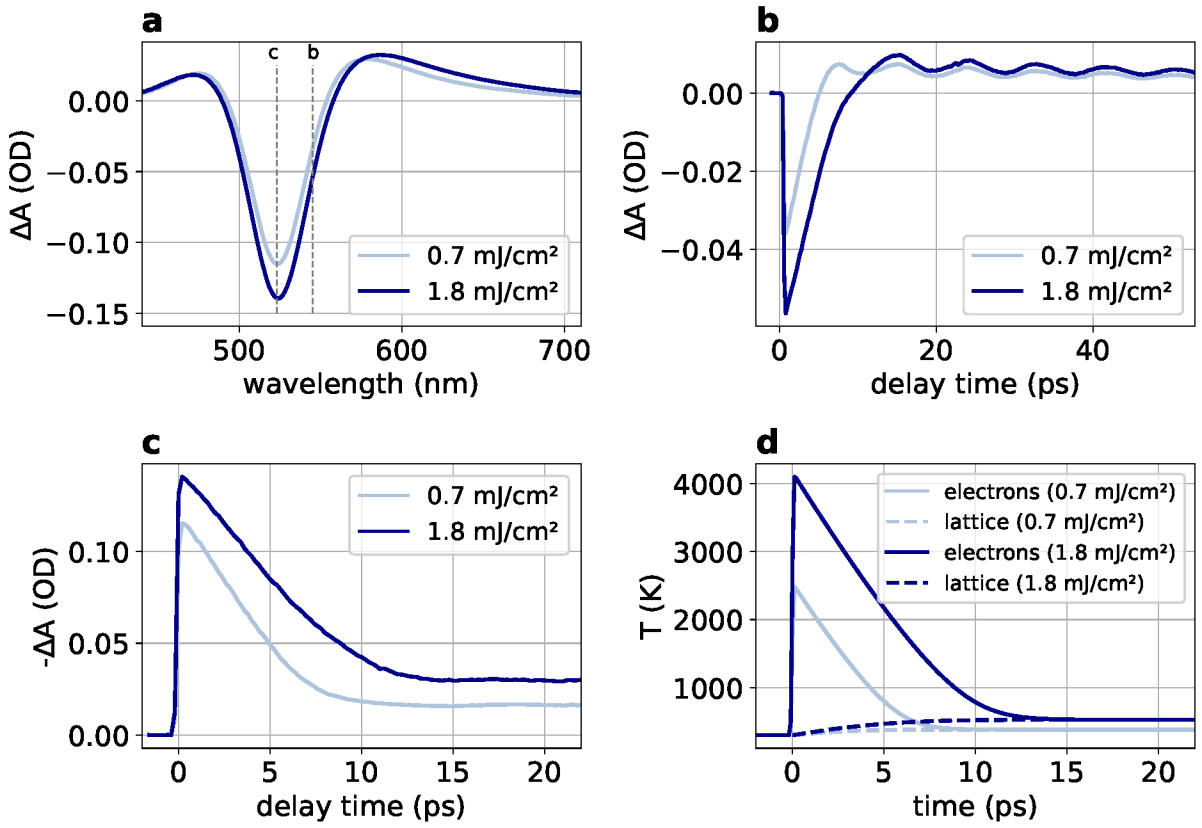

Figure 2: (a) TA spectra at the delay time of maximum contrast, i.e., 500 fs. The vertical dashed lines mark the probed wavelengths for b) and c). (b) TA kinetics probed at the bleach's long-wavelength shoulder (545 nm). (c) TA kinetics probed at the bleach centre-of-mass (ca. 525 nm). (d) Electron and lattice temperatures according to the two-temperature model (see Supporting Information Section 4).

Pump-probe spectroscopy of gold nanoparticles

We recorded the TA spectra of 27 nm, mono-crystalline, spherical AuNPs, stabilized in water with cetyltrimethylammonium chloride (see Supporting Information Section 1 for sample characterization). The excitation of the AuNPs with femtosecond laser pulses at a central wavelength of 400 nm led to TA spectra shown in Figure 2a. The shape of the spectra - a central bleach at the plasmon wavelength with positive sidebands - resulted from the change of the complex dielectric function of gold at elevated electron temperatures.[28]

AuNP size changes due to the breathing oscillations led to periodic modulations of the plasmon center wavelength, observable on the long-wavelength side of the TA spectrum (Figure 2b, Ref. 9). The temporal onset of the breathing oscillations were not visible, because the signal produced by hot electrons dominates the overall contrast.

Modeling the evolution of the electron temperature with a two-temperature model reproduced the TA bleach kinetics (Figure 2c-d). We conclude that the electron cooling time is excitation-fluence dependent and occurs on timescales of tens of picoseconds for the employed excitation conditions. As heat losses to the environment occur on much longer timescales, the lattice temperature increase can be assumed to coincide with the electron temperature decrease, Figure 2d.

Transient small-angle-x-ray-scattering

To assess the AuNP sizes in a direct fashion, we performed tSAX-SPI at the free-electron laser FLASH. Individual AuNPs were sequentially injected into the x-ray beam and excited with fs laser pulses of the same wavelength (400 nm) and fluence (0.7 and 1.8 mJ/cm^2) as for the TA experiments. The AuNP diameter changes were then probed by time-delayed ultrashort x-ray pulses. The serial nature of the measurement enabled the analysis of only those patterns which came from highly spherical particles. Any patterns which showed significant ellipticity were rejected (see Supporting Information for experimental and analysis details).

For both employed pump fluences we observed an immediate AuNP diameter expansion

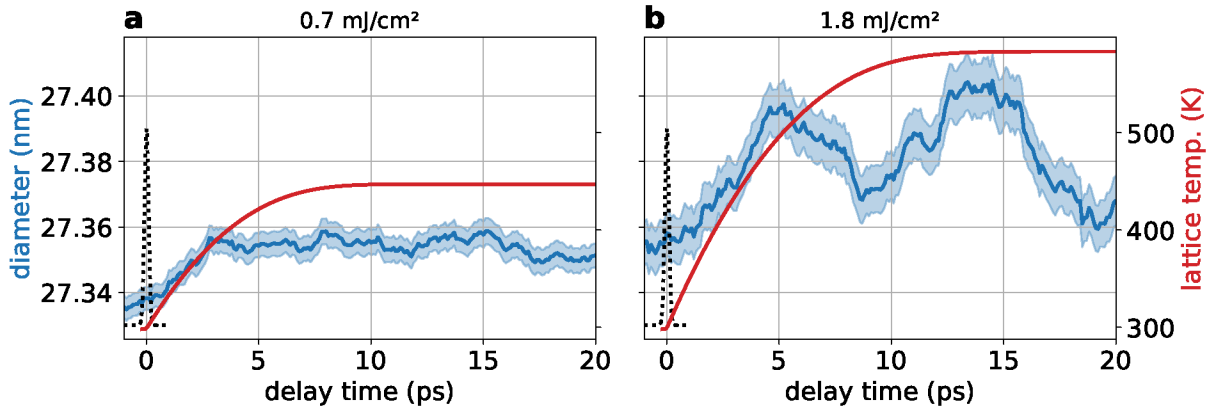

Figure 3: (blue) AuNP diameter according to tSAX-SPI experiment and (red) corresponding lattice temperatures according to a two-temperature model for two excitation fluences: (a) 0.7 mJ/cm^2 and (b) 1.8 mJ/cm^2. The shaded area is the AuNP diameter standard deviation. The envelope of the optical excitation pulse is indicated as dotted line.

with photoexcitation (Figure 3). An oscillation half cycle already occurred prior to the first oscillation being visible in the TA dynamics (cf. Figure 2b). The magnitude of the diameter increase was excitation-power dependent and the breathing oscillation was more clearly visible for the higher pump fluence of 1.8 mJ/cm^2. In Figure 3, we compare the experimental diameter oscillation with the lattice temperature obtained from the two-temperature model. The particle diameter reaches its maximum at a delay time of around 3 ps (5 ps) for a pump fluence of 0.7 mJ/cm^2 (1.8 mJ/cm^2) while the lattice temperature reaches its maximum at around 14 ps (17 ps). Considering the timescales, the thermal lattice expansion cannot be the main oscillation-driving impulsive source, since its rise time is longer than the breathing oscillation period.

Theory of electronic and thermal sources to the oscillation

To understand the origin of the breathing oscillations, we set up a fundamental microscopic model which extends earlier calculations in Ref. 24 to two-band models. We started with the definition of the lattice displacement at position $\mathbf{r}$ and time t as ob-

servable for the AuNP breathing oscillations, cf. S1:

$$\mathbf{u}_\beta(\mathbf{r},t) = \sum_{\mathbf{q}} \sqrt{\frac{\hbar}{2mN\omega_{\beta,\mathbf{q}}}} \mathbf{A}_{\beta,\mathbf{q}} e^{i\mathbf{q}\cdot\mathbf{r}} \left\langle b^\dagger_{\beta,-\mathbf{q}}(t) + b_{\beta,\mathbf{q}}(t) \right\rangle, \tag{1}$$

with the reduced Planck constant $\hbar$, phonon dispersion $\omega_{\beta,\mathbf{q}}$ and phonon annihilation (creation) operators $b^{(\dagger)}_{\beta,\mathbf{q}}$ with momentum $\mathbf{q}$ and branch β. Further, m accounts for an effective mass of the unit cell, $\mathbf{A}_{\beta,\mathbf{q}}$ for the polarization vector and N for the number of unit cells in the crystal. Focusing on the longitudinal acoustic (LA) phonon, $\beta = LA$, we calculated the equation of motion for the lattice displacement. The underlying Hamiltonian includes the electron-phonon interaction for a two-band model of the AuNP electrons including interband transitions as well as phonon-phonon interaction. (see Supporting Information Section 3). We obtain:

$$\left[\partial_t^2 + 2\gamma_p\partial_t - c_{LA}^2\nabla^2\right]\mathbf{u}(\mathbf{r},t) = \boldsymbol{\xi}[T(t) - T_0] + \zeta\,\nabla\rho^c(\mathbf{r},t). \tag{2}$$

The left-hand side accounts for a damped oscillator equation for the lattice displacement with the longitudinal velocity of sound c_{LA} and the damping rate γ_p. The right-hand side describes the sources of the lattice displacement: The thermal lattice expansion arises from the phonon-phonon interaction and accounts for the displacement of the equilibrium position as a function of the lattice temperature $T(t)$ with the coupling constant $\boldsymbol{\xi}$, cf. Figure 1 (red path). $T(t)$ was obtained by applying a two-temperature model (cf. Figure 2d and Supporting Information Section 3) and T_0 is the initial equilibrium temperature. Our microscopic approach revealed a second source term arising from the electron-phonon interaction. On the right-hand side of Eq. (2), the second term describes the excitation of coherent oscillations resulting from the optically-induced temporal buildup of the spatial gradient of the electron charge density $\nabla\rho^c(\mathbf{r},t)$ in the conduction band of the AuNP, cf. Fig 1 (blue path) and Supporting Information Section 3.

To connect the lattice diplacement with the optical excitation, we calculated the equation of motion for the conduction band electron density $\rho^c(\mathbf{r},t)$ [24,29–31] incorporating the

electron-light interaction and the electron-phonon interaction from the same Hamiltonian used above. In the limiting case of a short interband dephasing time compared to the pulse width, a rate equation for the electron density can be derived and expanded in orders of the exciting electric field, i.e. $\rho = \rho^0 + \rho^1 + \rho^2 + \mathcal{O}(E^3)$. We find that the densities are determined by a source term that scales with the electric field intensity:

$$\partial_t \rho_2^c(\mathbf{r}, t) = \frac{2e\epsilon_0}{\hbar} |\mathbf{E}(\mathbf{r}, t)|^2 \, \mathrm{Im}\{\chi^{\mathrm{inter}}(\omega_{\mathrm{opt}})\}, \tag{3}$$

where $\chi^{\mathrm{inter}}(\omega)$ is the interband contribution to the electric susceptibility of the AuNP, e is the elementary charge and ϵ_0 is the vacuum dielectric constant. Note that spatial gradients of the electron density are induced via the boundary conditions of Maxwell's equations for the self-consistently calculated electric field $\mathbf{E}(\mathbf{r}, t)$ showing amplification effects at the surface of the AuNP.

The coupled set of equations was solved by expansion into the vibrational eigenmodes of an oscillating sphere (Refs. 32, Supporting Information Section 3). Both, thermal and electron density source terms in Eq. 2 are indirectly initiated by the exciting optical field $\mathbf{E}(\mathbf{r}, t)$. However, the thermal contribution is delayed via the temporal buildup from non-equilibrium, whereas the electron density gradient is directly induced by the optical field. We found that the electron density gradient $\nabla \rho_2^c(\mathbf{r}, t)$ within the AuNP is the main source of the lattice displacement, since thermal expansion occurs with a time delay of a few ps and thus cannot explain the observed onset of the lattice displacement. Figure 4a shows the calculated evolution of the lattice displacement in comparison to the experimental data. We found an excellent agreement between experiment and theory. In particular, the onset – and thus the phase – of the breathing oscillations is well reproduced by our formalism. Figure 4b illustrates the temporal evolution of the two contributions (thermal and electronic) to the displacement. The contribution due to the spatial electron gradient starts immediately after the optical pulse since the electron density gradient scales with the electric field intensity, Eq. 3. On the timescales of the breathing oscillation and the electron cooling, the development of the electron density

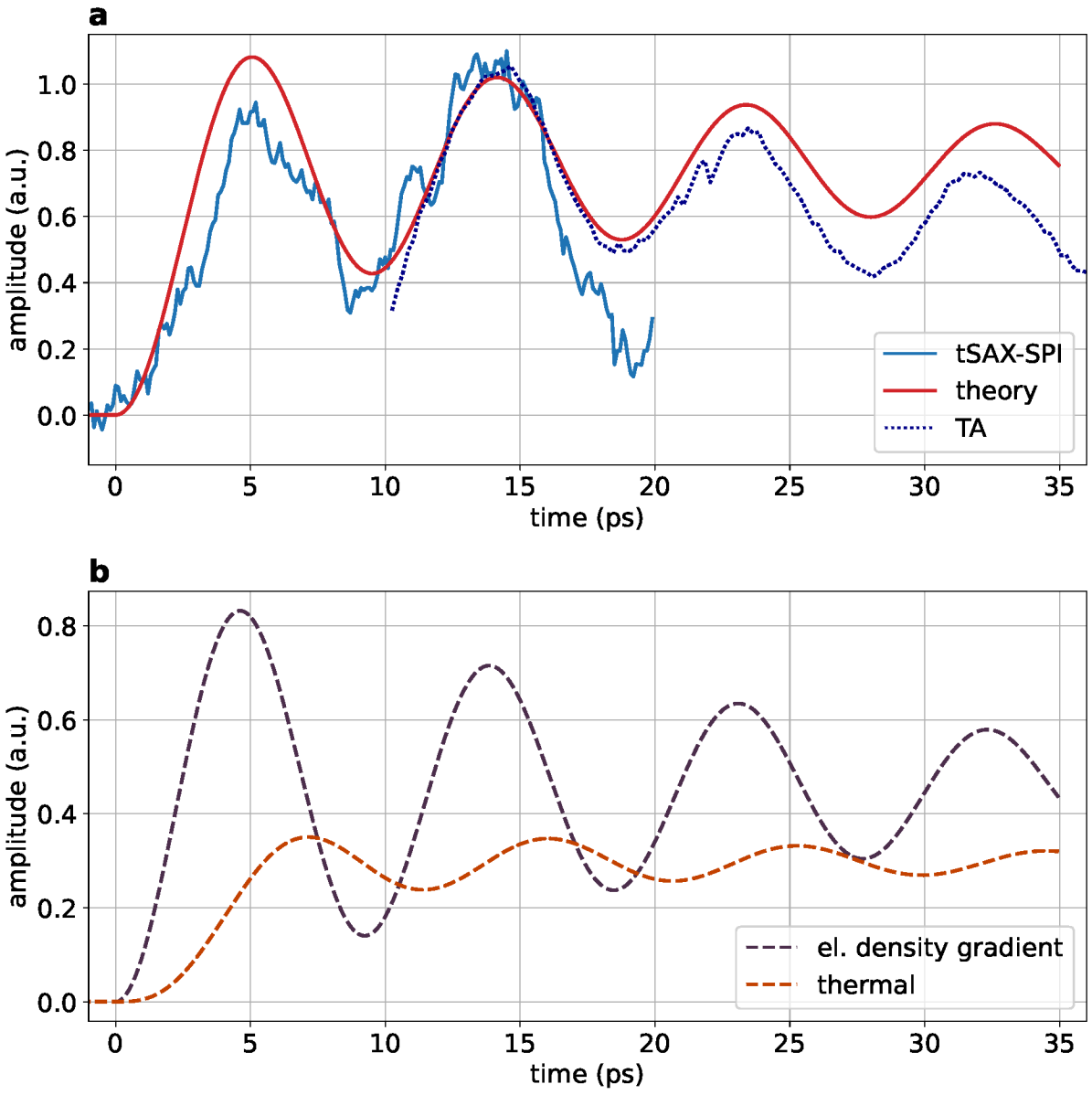

Figure 4: Experiment-theory comparison: (a), Particle size according to tSAX-SPI, TA kinetics at long-wavelength shoulder of the LSPR (the data is plotted for times after the initial electron cooling for better visibility and scaling.) and theoretical prediction of the particle diameter. The amplitudes were rescaled for easier comparability. (b), Relative contributions of electron density gradient and thermal expansion to the full theoretical prediction of the breathing oscillation.

gradient and the phonon excitation are simultaneous. The thermal expansion of the lattice also contributes to the excitation of the breathing oscillation, but to a lesser extent and on a slower timescale.

This is apparent also in the fluence-dependence: As the duration of the lattice temperature increase depends on the initial electron gas temperature (deposited energy) an excitation-fluence-dependent phase enters the temperature-based models.[9,33] Figure 5a displays TA data for the first resolvable breathing oscillations for increasing fluences. The fluence-dependent experimental data lacks any phase dependence. In the microscopic theory, the source term is dominated by electronic contributions, which show no fluence-dependent phase shifts, in agreement with the experiment. As expected, the thermal component shows a fluence-dependent phase, supporting the dominant relative contribution of the electronic excitation to the breathing oscillation.

Conclusion

Overall, we recorded time-resolved structural data of the AuNP breathing mode onset using single-particle imaging, which clearly confirm the necessity of two excitation sources for the breathing oscillations in AuNP, as was previously indicated indirectly from phase discrepancies. The combined time-resolved structural and optical data required the addition of direct interactions of the electronic system with coherent phonons to the excitation and phonon-lattice-coupling model, which were not only a necessary addition to the thermal driving terms but on short time scales indeed the dominant source term. Our theory quantitatively explains all experimental findings and provides general access to plasmon-lattice interaction. The concurrency of initial electron and lattice dynamics, caused by the immediate coupling of the optically-induced electron-density gradient and the breathing oscillation, might also have strong implications on energy transformations involving plasmonic hot carriers.

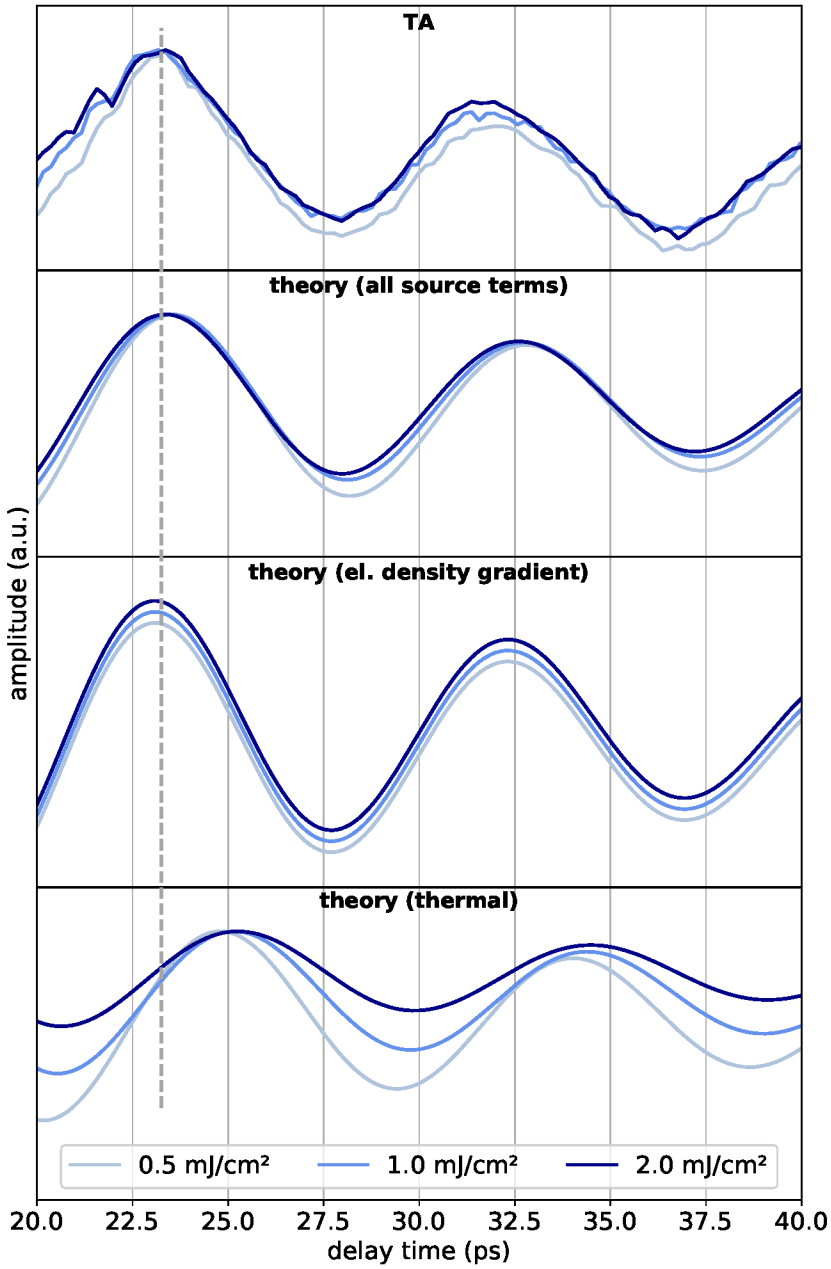

Figure 5: Experiment-theory comparison: Phase dependence on excitation fluence. TA data recorded for increasing pump fluences. "theory (all source terms)" includes both source terms in Eq. (2) while "theory (el. density gradient)" and "theory (thermal)" are expectation values if only one of the sources is considered, respectively. Theoretical data for the oscillation due to the electron density gradients include an offset for better visibility. All data were normalized to their maximum value. The maximum of the TA data is indicated by a dashed line for better visibility of the phase difference.

Data Availability

All data needed to evaluate the conclusions in the paper are present in the paper or the supplementary materials. Primary data is available from the corresponding authors upon reasonable request.

Supporting Information

Supporting Information with details on the following topics is available free of charge alongside this manuscript:

- Methods
- Data analysis of transient small-angle x-ray-scattering patterns
- Theory of electric and thermal sources to the oscillation
- Two-temperature model

Author Contributions

D.H. performed the TA experiments and synthesized the AuNPs together with F.S.; R.S. and M.S. developed the microscopic model, supervised by A.K.; L.W., J.L., A.D.E., K.D., and A.K.S. designed and performed the sample injection at the FEL. J.K. and A.K.S. devised and developed the XFEL experimental approach and designed and coordinated the experiment. The FEL experiment was set up and carried out by A.D.E., A.K.S., A.T.N., B.E., C.C.P., C.P., D.H., D.R., F.S., H.L., J.C., J.K., J.L., K.A., K.D., L.W., N.E., and Y.Z.; Y.Z. and K.A. analyzed the FEL data. K.A., J.K., and H.L. conceived the project and H.L. coordinated the project and drafted the manuscript together with D.H.. All authors contributed to the writing of the manuscript and the supporting material.

Acknowledgments

This work was supported by the German Research Foundation (DFG) by the federal cluster of excellence "Advanced Imaging of Matter" (EXC 2056, ID 390715994). We acknowledge the Deutsches Elektronen-Synchtrotron DESY, a member of the Helmholtz Association (HGF), for financial support as well as for the provision of experimental facilities and the Maxwell computational resources. Beamtime was allocated for proposal F-20190741. We acknowledge the Max Planck Society for funding the development and the initial operation of the CAMP end-station within the Max Planck Advanced Study Group at CFEL and for providing this equipment for CAMP@FLASH. The installation of CAMP@FLASH was partially funded by the BMBF grants 05K10KT2, 05K13KT2, 05K16KT3 and 05K10KTB from FSP-302. J.K. acknowledges support by the European Research Council through the Consolidator Grant COMOTION (614507). H.L., R.S., and M.S. acknowledge funding by the DFG (432266622).

References

(1) Reddy, H.; Wang, K.; Kudyshev, Z.; Zhu, L.; Yan, S.; Vezzoli, A.; Higgins, S. J.; Gavini, V.; Boltasseva, A.; Reddy, P.; Shalaev, V. M.; Meyhofer, E. Determining plasmonic hot-carrier energy distributions via single-molecule transport measurements. *Science* **2020**, *369*, 423–426.

(2) Tan, S.; Argondizzo, A.; Ren, J.; Liu, L.; Zhao, J.; Petek, H. Plasmonic coupling at a metal/semiconductor interface. *Nat Photon* **2017**, *11*, 806–812.

(3) Zhou, L.; Lou, M.; Bao, J. L.; Zhang, C.; Liu, J. G.; Martirez, J. M. P.; Tian, S.; Yuan, L.; Swearer, D. F.; Robatjazi, H.; Carter, E. A.; Nordlander, P.; Halas, N. J. Hot carrier multiplication in plasmonic photocatalysis. *Proc. Natl. Acad. Sci. U.S.A.* **2021**, *118*.

(4) Celiksoy, S.; Ye, W.; Wandner, K.; Kaefer, K.; Sönnichsen, C. Intensity-Based Single Particle Plasmon Sensing. *Nano Lett.* **2021**, *21*, 2053–2058.

(5) Mueller, N. S.; Okamura, Y.; Vieira, B. G. M.; Juergensen, S.; Lange, H.; Barros, E. B.; Schulz, F.; Reich, S. Deep strong light–matter coupling in plasmonic nanoparticle crystals. *Nature* **2020**, *583*, 780–784.

(6) Boriskina, S. V.; Cooper, T. A.; Zeng, L.; Ni, G.; Tong, J. K.; Tsurimaki, Y.; Huang, Y.; Meroueh, L.; Mahan, G.; Chen, G. Losses in plasmonics: from mitigating energy dissipation to embracing loss-enabled functionalities. *Adv. Opt. Photonics* **2017**, *9*, 775–827.

(7) Besteiro, L. V.; Yu, P.; Wang, Z.; Holleitner, A. W.; Hartland, G. V.; Wiederrecht, G. P.; Govorov, A. O. The fast and the furious: Ultrafast hot electrons in plasmonic metastructures. Size and structure matter. *Nano Today* **2019**, *27*, 120–145.

(8) Brongersma, M. L.; Halas, N. J.; Nordlander, P. Plasmon-induced hot carrier science and technology. *Nature Nanotech* **2015**, *10*, 25–34.

(9) Hartland, G. V. Optical Studies of Dynamics in Noble Metal Nanostructures. *Chem. Rev.* **2011**, *111*, 3858–3887.

(10) Linic, S.; Chavez, S.; Elias, R. Flow and extraction of energy and charge carriers in hybrid plasmonic nanostructures. *Nat. Mater.* **2021**, *20*, 916–924.

(11) Brown, A. M.; Sundararaman, R.; Narang, P.; Schwartzberg, A. M.; Goddard, W. A.; Atwater, H. A. Experimental and Ab Initio Ultrafast Carrier Dynamics in Plasmonic Nanoparticles. *Phys. Rev. Lett.* **2017**, *118*, 087401.

(12) Arbouet, A.; Del Fatti, N.; Vallee, F. Optical control of the coherent acoustic vibration of metal nanoparticles. *J. Chem. Phys.* **2006**, *124*, 144701.

(13) Ahmed, A.; Pelton, M.; Guest, J. R. Understanding How Acoustic Vibrations Modulate the Optical Response of Plasmonic Metal Nanoparticles. *ACS Nano* **2017**, *11*, 9360–9369.

(14) Yu, K.; Zijlstra, P.; Sader, J. E.; Xu, Q.-H.; Orrit, M. Damping of Acoustic Vibrations of Immobilized Single Gold Nanorods in Different Environments. *Nano Lett.* **2013**, *13*, 2710–2716.

(15) Perner, M.; Gresillon, S.; März, J.; von Plessen, G.; Feldmann, J.; Porstendorfer, J.; Berg, K.-J.; Berg, G. Observation of Hot-Electron Pressure in the Vibration Dynamics of Metal Nanoparticles. *Phys. Rev. Lett.* **2000**, *85*, 792–795.

(16) Wang, X.; Li, J.; Cao, J. Coherent phonon generation in laser-heated gold nanofilm. *J. Chem. Phys.* **2020**, *152*, 124704.

(17) Clark, J. N.; Beitra, L.; Xiong, G.; Higginbotham, A.; Fritz, D. M.; Lemke, H. T.; Zhu, D.; Chollet, M.; Williams, G. J.; Messerschmidt, M.; Abbey, B.; Harder, R. J.; Korsunsky, A. M.; Wark, J. S.; Robinson, I. K. Ultrafast Three-Dimensional Imaging of Lattice Dynamics in Individual Gold Nanocrystals. *Science* **2013**, *341*, 56–59.

(18) Clark, J. N.; Beitra, L.; Xiong, G.; Fritz, D. M.; Lemke, H. T.; Zhu, D.; Chollet, M.; Williams, G. J.; Messerschmidt, M. M.; Abbey, B.; Harder, R. J.; Korsunsky, A. M.; Wark, J. S.; Reis, D. A.; Robinson, I. K. Imaging transient melting of a nanocrystal using an X-ray laser. *Proc. Natl. Acad. Sci. U.S.A.* **2015**, *112*.

(19) von Reppert, A.; Sarhan, R. M.; Stete, F.; Pudell, J.; Del Fatti, N.; Crut, A.; Koetz, J.; Liebig, F.; Prietzel, C.; Bargheer, M. Watching the Vibration and Cooling of Ultrathin Gold Nanotriangles by Ultrafast X-ray Diffraction. *J. Phys. Chem. C* **2016**, *120*, 28894–28899.

(20) Shin, J.; Jung, C.; Ihm, Y.; Heo, S.-P.; Nam, D.; Kim, S.; Kim, M.; Eom, I.; Shim, J. H.; Noh, D. Y.; Song, C. Ultrafast Energy Transfer Process in Confined Gold Nanospheres Revealed by Femtosecond X-ray Imaging and Diffraction. *Nano Lett.* **2023**, *23*, 1481–1488.

(21) Gorkhover, T. et al. Femtosecond and nanometre visualization of structural dynamics in superheated nanoparticles. *Nature Photonics* **2016**, *10*, 93–97.

(22) Ayyer, K. et al. 3D diffractive imaging of nanoparticle ensembles using an x-ray laser. *Optica* **2021**, *8*, 15–23.

(23) Neutze, R.; Wouts, R.; van der Spoel, D.; Weckert, E.; Hajdu, J. Potential for biomolecular imaging with femtosecond X-ray pulses. *Nature* **2000**, *406*, 752–757.

(24) Salzwedel, R.; Knorr, A.; Hoeing, D.; Lange, H.; Selig, M. Theory of radial oscillations in metal nanoparticles driven by optically induced electron density gradients. *The Journal of Chemical Physics* **2023**, *158*, 064107.

(25) Sytwu, K.; Vadai, M.; Hayee, F.; Angell, D. K.; Dai, A.; Dixon, J.; Dionne, J. A. Driving energetically unfavorable dehydrogenation dynamics with plasmonics. *Science* **2021**, *371*, 280–283.

(26) Zhang, Y.; He, S.; Guo, W.; Hu, Y.; Huang, J.; Mulcahy, J. R.; Wei, W. D. Surface-Plasmon-Driven Hot Electron Photochemistry. *Chem. Rev.* **2018**, *118*, 2927–2954.

(27) Baffou, G.; Cichos, F.; Quidant, R. Applications and challenges of thermoplasmonics. *Nat. Mater.* **2020**, *19*, 946–958.

(28) Brown, A. M.; Sundararaman, R.; Narang, P.; Goddard, W. A.; Atwater, H. A. Ab initio phonon coupling and optical response of hot electrons in plasmonic metals. *Phys. Rev. B* **2016**, *94*, 075120.

(29) Grad, H. On the kinetic theory of rarefied gases. *Commun. Pure Appl. Math.* **1949**, *2*, 331–407.

(30) Gardner, C. L. The quantum hydrodynamic model for semiconductor devices. *SIAM J. Appl. Math.* **1994**, *54*, 409–427.

(31) Cai, Z.; Fan, Y.; Li, R.; Lu, T.; Wang, Y. Quantum hydrodynamic model by moment closure of Wigner equation. *J. Math. Phys.* **2012**, *53*, 103503.

(32) Lamb, H. On the vibrations of an elastic sphere. *Proc. London Math. Soc.* **1881**, *1*, 189–212.

(33) Voisin, C.; Del Fatti, N.; Christofilos, D.; Vallée, F. Time-resolved investigation of the vibrational dynamics of metal nanoparticles. *Appl. Surf. Sci.* **2000**, *164*, 131–139.